Hydrogenation of CO2 to Methanol by Pt Nanoparticles Encapsulated in UiO-67: Deciphering the Role of the Metal−Organic Framework

Emil S. Gutterød,[†] Andrea Lazzarini,[†] Torstein Fjermestad,[‡] Gurpreet Kaur,[†] Maela Manzoli,[§] Silvia Bordiga,[†,‖] Stian Svelle,[†] Karl P. Lillerud,[†] Egill Skúlason,[⊥] Sigurd Øien-Ødegaard,[†] Ainara Nova,[‡] and Unni Olsbye*,[†]

[†]Centre for Materials Science and Nanotechnology, Department of Chemistry, University of Oslo, Sem Saelandsvei 26, N-0315 Oslo, Norway

[‡]Hylleraas Centre for Quantum Molecular Sciences, Department of Chemistry, University of Oslo, P.O. Box 1033, Blindern, N-0315 Oslo, Norway

[§]Department of Drug Science and Technology and NIS, Centre for Nanostructured Interfaces and Surfaces, University of Turin, Via P. Giuria 9, 10125 Turin, Italy

[‖]Department of Chemistry, NIS Interdepartmental Centre and INSRM Reference Centre, University of Turin, via Quarello 15A, I-10135 Turin, Italy

[⊥]Science Institute and Faculty of Industrial Engineering, Mechanical Engineering and Computer Science, University of Iceland, VR-III, 107 Reykjavik, Iceland

S *Supporting Information*

ABSTRACT: Metal−organic frameworks (MOFs) show great prospect as catalysts and catalyst support materials. Yet, studies that address their dynamic, kinetic, and mechanistic role in target reactions are scarce. In this study, an exceptionally stable MOF catalyst consisting of Pt nanoparticles (NPs) embedded in a Zr-based UiO-67 MOF was subject to steady-state and transient kinetic studies involving H/D and $^{13}C/^{12}C$ exchange, coupled with operando infrared spectroscopy and density functional theory (DFT) modeling, targeting methanol formation from CO_2/H_2 feeds at 170 °C and 1−8 bar pressure. The study revealed that methanol is formed at the interface between the Pt NPs and defect Zr nodes via formate species attached to the Zr nodes. Methanol formation is mechanistically separated from the formation of coproducts CO and methane, except for hydrogen activation on the Pt NPs. Careful analysis of transient data revealed that the number of intermediates was higher than the number of open Zr sites in the MOF lattice around each Pt NP. Hence, additional Zr sites must be available for formate formation. DFT modeling revealed that Pt NP growth is sufficiently energetically favored to enable displacement of linkers and creation of open Zr sites during pretreatment. However, linker displacement during formate formation is energetically disfavored, in line with the excellent catalyst stability observed experimentally. Overall, the study provides firm evidence that methanol is formed at the interface of Pt NPs and linker-deficient Zr_6O_8 nodes resting on the Pt NP surface.
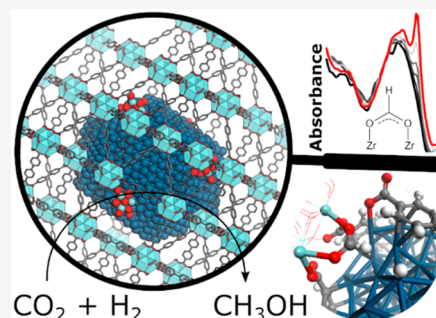
INTRODUCTION

Atmospheric levels of CO_2 have risen at an alarming rate since the first half of the 20th century following our continuous and increasing use of fossil fuels. Large cuts in CO_2 emissions can be made through utilization of greener alternatives of energy production such as solar and wind power; however, these energy sources suffer from the lack of continuity in energy output and require efficient methods for large scale energy storage in order to compete with fossil fuels.[1] One of the solutions to this problem is the production of easily stored liquid fuels with high volumetric and gravimetric energy density, such as methanol, from CO_2 and green hydrogen.[2] This allows for continued use of an already existing

infrastructure.[3] Substantial research efforts have already been dedicated to the topic of valorizing CO_2 through hydrogenation, mainly with focus on the reverse water−gas shift (RWGS) reaction, methanation, and methanol production.[4−13]

The product distribution of CO_2 hydrogenation varies significantly with the nature of the catalyst and operating conditions.[7] Most prior studies show that Pt-based systems are highly selective for the RWGS reaction with a minor selectivity toward methane.[11,14−19] In that respect, Kattel et al.[18] performed a computational study of CO_2 hydrogenation over

Pt nanoparticles supported on SiO_2 and TiO_2. They concluded that a RWGS and CO hydrogenation path, forming CO and small amounts of methane, dominates over those materials. This finding is in agreement with experimental evidence of CO formation mainly via surface carbonates.[15,16]

Surface formates are also observed in several studies of the RWGS[15,16,20,21] and of water gas shift (WGS)[22−24] reactions; however, the significance of such a pathway over Pt-based catalysts is debated. In this regard, Burch et al.[23] conducted a critical analysis of the experimental evidence for and against a formate mechanism over highly active Pt and Au WGS catalysts. They argue that most published results do not provide definite evidence for or against a formate pathway for the WGS reaction, and in the cases where reliable data are available, it is at most a minor and slow reaction pathway.

Recent studies show that, when supporting Pt on a methane producing Co-oxide catalyst, methanol selectivity is observable under favorable conditions of low temperature and elevated pressure.[25−27] Furthermore, one prior study[28] demonstrated selectivity toward methanol over oxide-supported Pt where the supports alone are inactive in CO_2 hydrogenation: out of a set of catalysts producing mainly CO (>91%), Pt/ZrO_2 showed the highest CH_3OH selectivity, reaching 6% at 200 °C and 10 atm pressure.

Over the Zr−metal−organic frameworks (MOFs) UiO-66 and -67, functionalized with Cu and Cu/Zn, high methanol selectivity is ascribed to an important role of the Zr−MOF interface in the reaction. Rungtaweevoranit et al.[29] found XPS evidence of Zr reduction in the presence of Cu when studying Cu nanoparticles (NPs) deposited on UiO-66 as a model system for the encapsulated version of the catalyst (i.e., Cu in UiO-66). Similar findings from XPS on CuZn@UiO-67 samples with 100% bipyridine-type linkers treated with reaction gas showed indications of Zr(IV) reduction to Zr(III), suggested to be caused by H adsorption.[30] In combination with H_2- and CO_2-TPD results, the authors suggested participation of the Zr cluster in the reaction by means of H spillover from Cu and CO_2 adsorption on unsaturated Zr sites. When the catalyst was prepared with regular UiO-67 (i.e., biphenyl-type linkers), both the CH_3OH selectivity and catalytic stability decreased. Although the CuZn@UiO-67 material showed substantial activity in methanol formation, notably, both the crystallinity and specific surface area of the MOF were severely reduced already by the deposition of copper. Thus, the material did not exhibit the well-defined MOF structure of UiO-67 during the subsequent experiments.[30]

In a previous contribution, we reported the CO_2 hydrogenation activity and selectivity of an exceptionally stable Pt Zr−MOF catalyst, UiO-67-Pt, at ambient pressure. This catalyst maintains its well-defined MOF structure even after long-term operation and is therefore well suited as a model system for studying the influence of the MOF framework on the reaction. In the current study, the focus is set on elucidating the role of the UiO-67 framework in CO_2 hydrogenation to methanol through a kinetic investigation. In addition to standard steady-state kinetic measurements, we employ H/D- and $^{13}C/^{12}C$ SSITKA and operando FT-IR measurements, methods scarcely employed in MOF catalysis literature. In combination with density functional theory (DFT) calculations, this work reveals unprecedented insight in the Pt−Zr−MOF interplay that leads to methanol formation during conversion of CO_2/H_2 mixtures at 170 °C and 1−8 bar.

EXPERIMENTAL DETAILS

Details of material preparation and standard characterization methods (N_2 adsorption, ^1H NMR, EDX, TGA, TEM, and CO-chemisorption) are provided in the Supporting Information.

Operando FT-IR spectroscopy was performed using a Bruker Vertex70 instrument equipped with a liquid nitrogen-cooled MCT detector. Each spectrum was collected by averaging 64 acquisitions with a resolution of 2 cm^{-1}. The sample (pressed in a self-sustained pellet of approximately 4 mg) was mounted inside a low free-volume cell from AABSPEC (model #CXX), by which pressure, temperature, and gas flow are controllable. Due to the low sample amount, the CO_2 conversion was too low to be determined reliably, and parallel experiments under comparable conditions were performed with the focus on gas-phase analysis (vide infra). The sample was activated at 350 °C (5 °C/min ramp) in 10% H_2/He (10 mL/min) for 4 h and then cooled to 170 °C in 10 mL/min He. The sample was kept under CO_2 hydrogenation (CO_2/H_2 = 1/6, 10 mL/min) reaction conditions for 2 h, before the H_2 flow was exchanged to D_2.

Catalytic testing was performed in a fixed-bed flow setup with a straight stainless steel reactor (7 mm I.D.) operated under 1−8 bar, where effluent species is analyzed with an online Q-MS (Pfeiffer) and GC-TCD-FID (Agilent). The MOF samples were reduced for 4 h at 350 °C (5 °C/min ramp) in 20 mL/(min·0.1 g$_{cat}$) flow of 10% H_2/Ar under ambient pressure. Following the activation procedure, the reactor was cooled to 240 °C in inert flow and then operated for 4 h reaching steady state under a set of reference conditions (1/6/3 CO_2/H_2/inert, 20 mL/min, 200 mg, τ = 0.01 g$_{cat}$·min/mL and ambient pressure) before changing conditions. The prereduced commercial samples Pt/SiO_2 (abcr), Pt/Al_2O_3 (Chimet), and Pt/C (Chimet) were heated directly to 240 °C under reference conditions, which were maintained until steady state was reached. Dependent on the experimental aim, 0.05−0.2 g of catalyst was tested for CO_2 hydrogenation in the range of 5−25% CO_2, 40−90% H_2, T = 170 °C, p = 1−8 bar, and contact time (τ) = 0.004−0.04 g$_{cat}$·min/mL. A given set of operating conditions was fixed until steady state was reached and for at least 2 h. During kinetic studies, changes in reaction conditions were performed in a random sequence. Each 3−4 set of conditions were the reference conditions. They showed that the change in catalyst performance was negligible during the kinetic studies. As reported in ref 17, a minor increase in the catalytic activity and change in selectivity is observed for UiO-67-Pt during long-term operation. The same procedure as described above was followed in the H/D exchange experiments but with D_2 instead of H_2. H/D SSITKA experiments were performed by operating the catalysts at steady state under reference conditions and then switching the feed (1/6/3 CO_2/H_2/inert) rapidly to another feed containing D_2 instead of H_2 (1/6/3 CO_2/D_2/inert) using an electronically controlled 4-port 2-way valve. Switches back and forth between the two feeds were performed in intervals of 8 h. $^{13}CO_2/^{12}CO_2$ SSITKA experiments were performed in the same manner. The m/z values traced for each specie in the respective experiments are tabulated in Table S1.

Intermediates and catalyst structures were optimized using DFT calculations. The calculations were carried out using the mixed Gaussian and plane wave method[31−33] as implemented in CP2K 6.1.[34,35] The functional was PBE+D3; the atom-centered basis set was DZVP-MOLOPT-SR-GTH,[36] and the plane wave kinetic energy cutoff was 360 Ry. Further details are provided in the Supporting Information.

RESULTS AND DISCUSSION

The UiO-66 series of Zr−MOFs (UiO-66, −67, −68) consists of Zr_6O_8 nodes connected by dicarboxylate-terminated linkers. The ideal linker-to-node ratio is 6:1, but prior investigations showed that factors like synthesis conditions (type of modulator and concentration, temperature, and crystallization time) and activation conditions may strongly affect this ratio, leading to materials that are commonly referred to as having "missing cluster" or "missing linker" defects, respectively.[37−43]

Scheme 1. (Left) TEM Micrograph Showing the Close Packed (111) Layers of Zr_6O_8 Clusters in UiO-67, with a Spacing of 15.5 Å[a]. (Right) A 1600 Atom Pt NP in UiO-67 Viewed in the Same Direction[b]
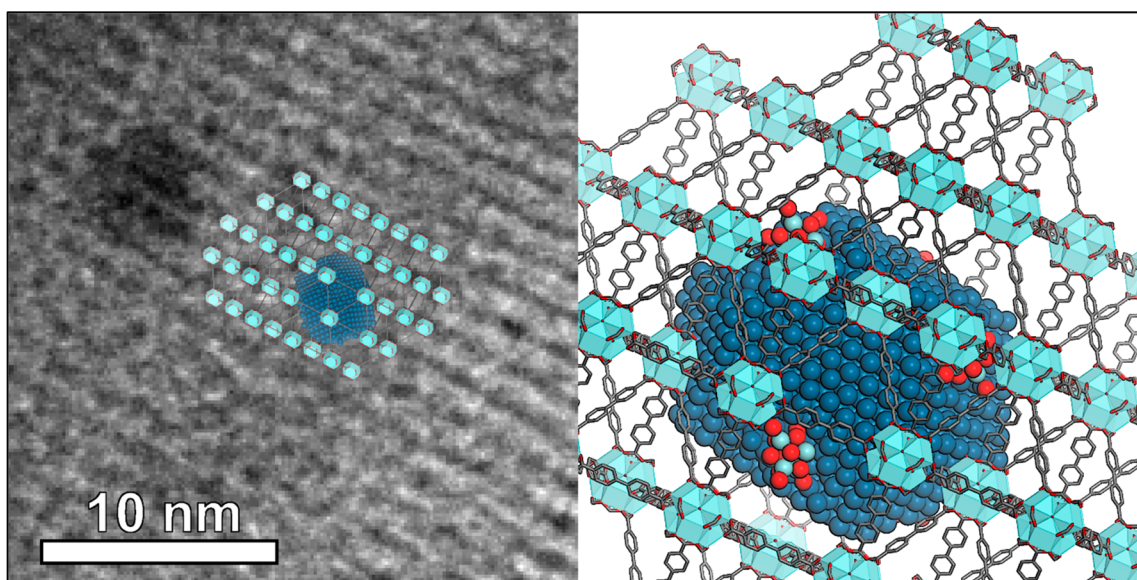
[a]The TEM Micrograph is overlaid with a 1600 Atom Pt NP in the Structure of UiO-67 Viewed along (112), Which Is Perpendicular to (111). [b]Six Zr_6O_8 clusters have been decoupled from the MOF lattice to accommodate the NP and are decorating the NP surface.
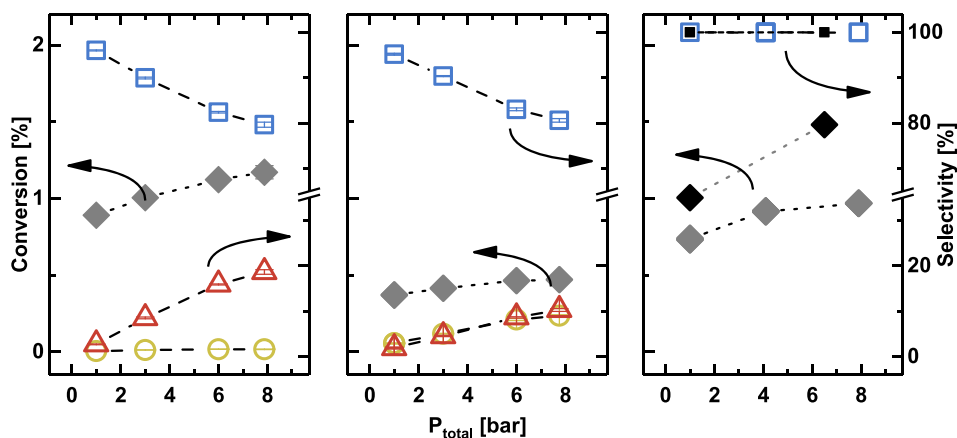

Figure 1. CO_2 conversion (left axes, diamonds) and product selectivity (right axes) during CO_2 hydrogenation under 1−8 bar total reaction pressure and T = 170 °C. (Left) UiO-67-Pt. (Middle) Pt/Al_2O_3. (Right) Pt/SiO_2 (gray, blue) and Pt/C (black). CO, CH_4, and CH_3OH selectivity is depicted as squares, circles, and triangles, respectively. τ = 0.01 g_{cat}·min/mL, CO_2/H_2/inert = 1/6/3. For Pt/Al_2O_3, τ = 0.02 g_{cat}·min/mL.

Missing linker defects may be capped by modulator, anions of the MOF precursor salts, solvent, or OH^-/H_2O pairs.[39,42,44,45]

The current study was carried out using UiO-67 with 90% biphenyl-4,4′-dicarboxylic acid (BPDC) linkers and 10% 2,2′-bipyridine-5,5′-dicarboxylic acid (BPYDC) linkers, hereafter called UiO-67-Pt. Prior studies have demonstrated that the bipyridine entity in BPYDC is the preferred anchoring site for Pt salts in this MOF.[17,46−48] In the current study, ^{1}H NMR analysis of digested material showed that the as-synthesized MOF contained 11 BPYDC linkers, 13 benzoic acid ligands, and 2 formic acid ligands, respectively, per 100 BPDC linkers (Table S3). Furthermore, thermogravimetric analysis (TGA) measurements indicated that the as-synthesized MOF had a linker-to-node ratio of 5, suggesting that, in addition to benzoic acid and formic acid, the material contained Cl^- or OH^-/H_2O pairs, adding up to an average of 4 out of 24 Zr coordination sites per Zr node that were not connected to a linker molecule (Table S3).

After wet impregnation with the Pt NP precursor, K_2PtCl_4, the BPYDC and benzoic acid contents of UiO-67-Pt decreased slightly, while the formic acid content increased to 4 per 100 BPDC linkers (Table S2). Activation in a reducing atmosphere (10% H_2/Ar flow at 350 °C, 1 bar, 4 h) transformed the Pt precursor salt into the active catalytic entity for CO_2 hydrogenation, Pt NPs.[17,46,48] In the current case, transmission electron microscopy (TEM) investigations after activation showed the presence of Pt NPs homogeneously dispersed within the MOF framework (Figure S5). The Pt NPs supported on UiO-67 have average diameter of 3.6 ± 0.7 nm (Figure S5), i.e., larger than the diameter of the tetrahedral (1.2 nm) and octahedral (2.3 nm) cavities of the UiO-67 structure. Most of the Pt NPs displayed a spherical shape; however, careful inspection revealed the presence of NPs with squared borders and an irregular shape, possibly exposing well-defined terraces, after activation and after reaction (Figures S5 and S6). Such features can arise from strong Pt−support

Table 1. Pt Amount, NP Diameter (d_{NP}), CO Uptake ($N_{A,CO,RT}$), Estimated Exposed Pt Surface ($N_{surf,Pt}$), and the Amount of HD Formed ($N_{A,HD}$) after Switching from $H_2 + CO_2$ to $D_2 + CO_2$ at 170 °C, 1 bar

Catalyst	Pt amount (wt %)	d_{NP} (nm)	$N_{A,CO,RT}$[c] (μmol/g$_{cat}$)	$N_{surf,Pt}$[d] (μmol/g$_{cat}$)	$N_{A,HD}$ (μmol/g$_{cat}$)
UiO-67-Pt	2.7[a]	3.6 ± 0.7	1.7 ± 0.3	55	1200
Pt/Al$_2$O$_3$	5[b]	1.4[b]	36	200	1100
Pt/SiO$_2$	5[b]	5 ± 2	13	76	540
Pt/C	5[b]	2[b]			

[a]Theoretical amount of impregnation. A Pt amount of 2.4 ± 0.4 wt % was estimated from EDX analysis (see the Supporting Information). [b]Obtained from the provider. [c]Pulse-chemisorption at room temperature. [d]Estimated from TEM by following the procedure described in the Supporting Information.
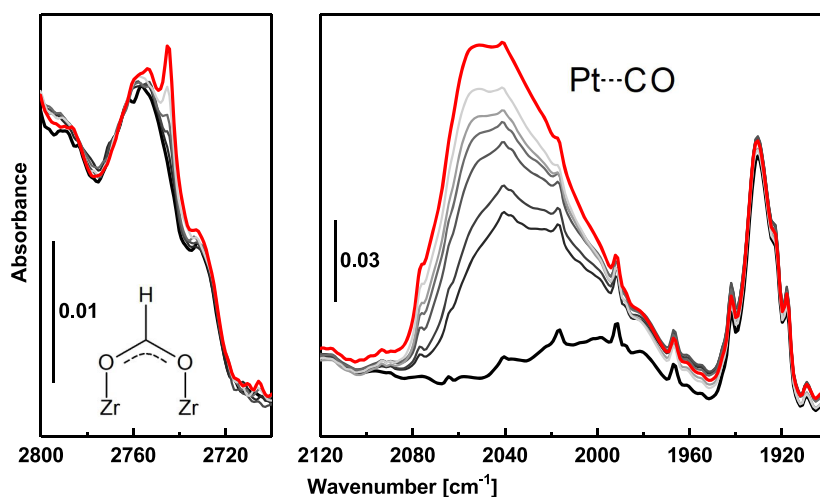

Figure 2. FT-IR spectra of UiO-67-Pt collected during CO_2 hydrogenation ($CO_2/H_2 = 1/6$, 10 mL/min, 170 °C, 1 bar) at different times (thick black curve for $t = 0$ min, gray scale from darkest to brightest for $0 < t < 120$ min, thick red curve for $t = 120$ min). The left figure shows the magnified spectral region of the ν(C−H) for formate groups, while the right figure depicts the spectral interval typical for CO linearly adsorbed on metal nanoparticles. Full range spectra are reported in Figure S16.

interaction, and indeed, limited broadening of the Pt NP size distribution was observed after prolonged testing (Figure S6). A schematic illustration of a 3.6 nm Pt particle embedded in an 8 unit cell-enclosed octahedral cavity, mimicking a representative Pt NP observed by TEM, is presented in Scheme 1.

CO_2/H_2 conversion and product selectivity obtained over Pt/C, Pt/SiO$_2$, Pt/Al$_2$O$_3$, and UiO-67-Pt at 170 °C and 1−8 bar are shown in Figure 1. Substantial selectivity differences were observed at similar conversion levels (0.4−1.5%): Over UiO-67-Pt, the methanol selectivity increased from around 3% to 19%, corresponding to a turnover frequency (TOF) of 0.01 s^{-1}, when the pressure increased from 1 to 8 bar (Figure 1). This is, to the best of our knowledge, the second report of significant methanol formation from CO_2 over a Pt-based catalyst where the support alone is inactive in the reaction.[28] Under the same conditions, there was only a slight increase in methane selectivity from 1.2% to 1.6%. Over Pt/Al$_2$O$_3$, both the methane and methanol selectivity reached 10% under 8 bar pressure (Figure 1). In contrast to UiO-67-Pt, methane selectivity increased substantially with increasing pressure. Finally, over Pt/SiO$_2$ and Pt/C (Figure 1), CO was the only carbon-containing product observed, in accordance with the theory predictions of Kattel et al. for unsupported Pt NPs.[18] The formation of methanol over UiO-67-Pt points to strong metal−support interactions, as previously reported for Cu NPs embedded in UiO Zr−MOFs[29,30] and may suggest that the MOF support plays an active role during the reaction, similarly to Al$_2$O$_3$ in the WGS and CO_2 hydrogenation reactions.[8,24,49]

To further assess the role of Pt NPs vs support in CO_2 hydrogenation, steady-state H_2/D_2 exchange experiments were performed under CO_2 hydrogenation conditions over UiO-67-Pt, Pt/Al$_2$O$_3$, Pt/SiO$_2$, UiO-67, and SiO$_2$. The transient evolution of the HD molecule following a feed switch from $CO_2 + H_2$ to $CO_2 + D_2$ is shown in Figure S9. Importantly, the formation of HD (and other products) was observed only over the Pt containing materials but not over the UiO-67 and SiO$_2$ supports alone, showing that the dissociation of H_2/D_2 only occurs when Pt is present. The amount of HD formed over UiO-67-Pt and Pt/Al$_2$O$_3$ was larger than that over Pt/SiO$_2$ and, in all cases, 1−2 orders of magnitude higher than the amount of exposed Pt atoms in Pt nanoparticles (Table 1). This observation, in combination with the observed HD tailing, strongly suggests H/D exchange with hydroxyl groups on the support materials, either directly by hydrogen spillover to/from the Pt NPs or by H/D exchange with the water molecules formed during the reaction.

Insights into the origin of HD tailing and formed amount over the UiO-67-Pt sample were obtained by a parallel operando FT-IR experiment under comparable conditions (1 bar, 170 °C, $CO_2/H_2 = 1/6$). When exchanging H_2 for D_2, the sharp signal of Zr−μ_3-OH at 3669 cm^{-1}[39] decreased to zero with time while another equally sharp and intense peak, corresponding to the deuterated species Zr−μ_3-OD, increased at 2705 cm^{-1} (Figure S16). Interestingly, the quantification of the molar number of H in HD, $N_{A,HD}$, yields 1200 μmol H per gram catalyst, which corresponds to about 70% of the theoretical number of Zr−μ_3-OH groups in the sample. No
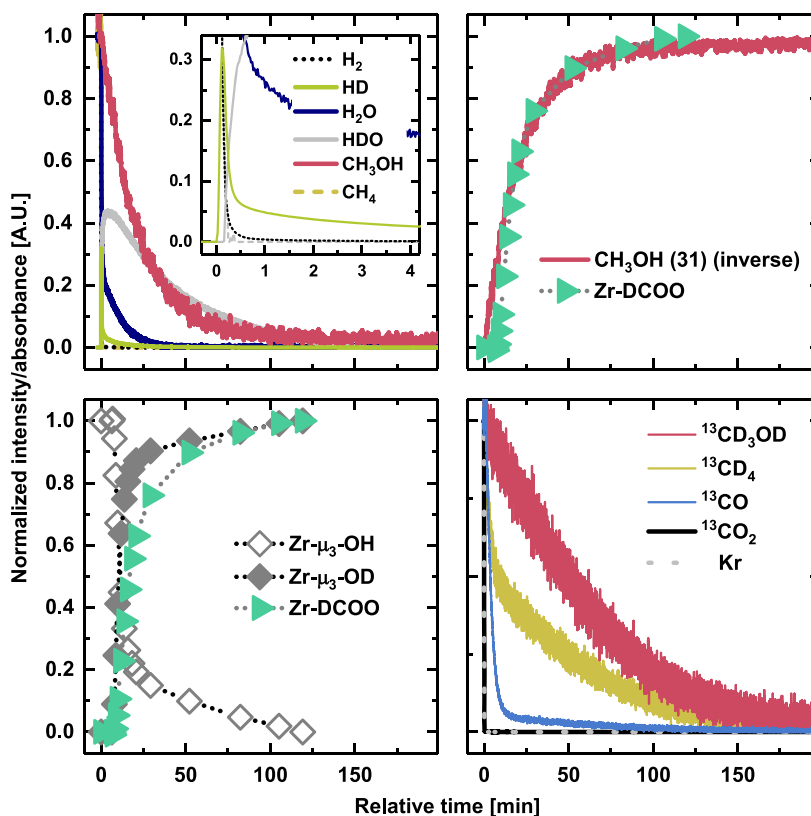
Figure 3. (Top left) Normalized intensity of H_2 ($m/z = 2$), HD ($m/z = 3$), H_2O ($m/z = 18$), HDO ($m/z = 19$), CH_3OH ($m/z = 31$), and CH_4 ($m/z = 15$) when switching from $CO_2 + H_2$ to $CO_2 + D_2$ at $t = 0$. (Top right) Comparison of Zr-DCOO and CH_3OH (inverse) during H/D exchange. (Bottom left) Normalized absorbance of Zr$-\mu_3$-OH (open diamonds), Zr$-\mu_3$-OD (filled diamonds), and deuterated formate (triangles) during the exchange of H_2 to D_2 at steady-state CO_2 hydrogenation. $CO_2/H_2(D_2) = 1/6$, 10 mL/min, 170 °C, 1 bar. (Bottom right) Normalized intensity of Kr ($m/z = 84$), $^{13}CO_2$ ($m/z = 45$), ^{13}CO ($m/z = 29$), $^{13}CD_4$ ($m/z = 21$), and $^{13}CD_3OD$ ($m/z = 35$) products when switching from $^{13}CO_2 + D_2$ to $^{12}CO_2 + D_2$ at $t = 0$. $T = 170$ °C, 1 bar, $\tau = 0.01$ g_{cat}·min/mL.

other indication of H/D exchange (neither on Pt nor in linkers) was found from the FT-IR experiments. A more detailed description of the spectra obtained during FT-IR experiments over UiO-67-Pt, including the hydroxyl group region and the C−H bonds present in the aromatic linkers (the carboxylates region is omitted as it is out of scale), is given in the supporting section (Figure S16). It is important to note that the chemical integrity of the catalyst is preserved during the reaction, and changes in the spectra are therefore caused by reaction products interacting with the sample. The most evident change is caused by the progressive increase of CO on the Pt nanoparticles (Figure 2). The shape and frequency of this signal is compatible with carbonyls linearly adsorbed on Pt atoms at the surface of the NPs, as we already addressed in our previous study on an analogous material.[17] The size of the particles (3.6 nm) and the temperature (170 °C) justify the absence of bridged carbonyl species at lower frequencies. Changes in one of the smaller peaks in the IR spectra are the most novel observation of this study: the peak arising at 2745 cm^{-1} (Figure 2) is due to the appearance of bidentate formate groups[39] (which, notably, are absent after activation; see Figure 2), most likely coming from the progressive process of the CO_2 reduction. The frequency of this weak feature is compatible with the $\nu_s(COO) + \delta(CH)$ vibration of bidentate formates directly connected to open Zr sites of the Zr nodes in the MOF framework.[39,50,51] Further bands associated with formate are visible in the top part of Figure S16 in the 3000−2800 cm^{-1} region. The spectrum of the sample collected during CO_2

hydrogenation after the subtraction of the activated one (Figure S17) highlights the formation of four additional bands at 2910, 2888, 2868, and 2854 cm^{-1}, ascribable to various formate species at the Zr node.[39] This is, to the best of our knowledge, the first report of formate formation at the MOF Zr node under CO_2 hydrogenation reaction conditions.

The importance of these moieties is even more evident, thanks to the isotopic exchange experiment between H_2 and D_2. When exchanging H_2 for D_2, the signals of the formate groups shifted to lower wavenumbers; the signals in the 2950− 2850 cm^{-1} region shifted to the region of the CO_2 roto-vibrational profile and are therefore not detectable. Conversely, the band at 2745 cm^{-1} shifted to 2168 cm^{-1}[39] (Figure S16) and the intensity vastly increased as compared to the H-analogue ($I_{HCOO}/I_{DCOO} \approx 0.02$). The intensity increase indicates an inverse kinetic isotope effect, although possible differences in the extinction coefficient of the two species cannot be excluded. Importantly, a corresponding, gradual increase in methanol production rate was observed upon H_2/ D_2 exchange under steady-state CO_2 hydrogenation conditions (Figure S14). At isotope equilibration, this difference in H- and D-methanol production rates corresponds to an inverse kinetic isotope effect (KIE), $r_H/r_D = 0.36$. Moreover, the temporal scale of exchange was very similar for the formate species and for methanol in the parallel H_2/D_2 exchange experiments performed in the FT-IR transmission cell and the test setup, respectively (Figure 3) (see the Experimental Details for more information). Together, these experiments provide firm

Scheme 2. Schematic Presentation of the Postulated Reaction Mechanism of CO_2 Hydrogenation to the Formate Intermediate in CH_3OH Formation at the Pt−Zr Node Interface
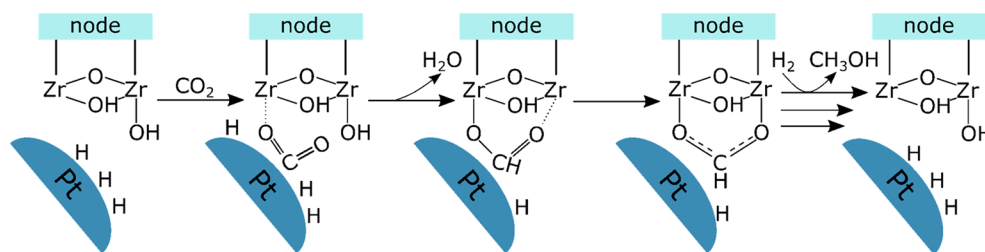
evidence that the Zr−formate species is a key intermediate in the methanol formation path.

Furthermore, during a complementary $(^{13}CO_2 + D_2)/$ $(^{12}CO_2 + D_2)$ exchange experiment (Figure 3), $^{13}CD_3OD$ decreased steadily to zero in about 200 min, similarly to what was observed for formate and methanol during the H_2/D_2 switch. The slope of the normalized intensity of methanol in a semi-logarithmic plot (Figure S15) is inversely proportional to the mean surface residence time $(-1/\tau_{res})$ of intermediates leading to the formation of methanol (Table 3) and is characteristic of the formation from a single pool of intermediates.[52]

Overall, the transient experiments provide firm evidence that formate species, attached to the Zr nodes in a bidentate configuration, are formed by H transfer from an adjacent Pt NP. The inverse KIE observed for methanol formation (r_H/r_D = 0.36) is a signature of reactions where the rate limiting step involves hydrogen addition to an sp- or sp^2-hybridized carbon, leading to a hybridization change (sp to sp^2 or sp^2 to sp^3).[10,53] CO_2 hydrogenation to methanol via formate species involves two such steps: CO_2 hydrogenation to form formate, and formate hydrogenation to (probably) form dioxymethylene.[54] The observation of abundant formate species by FT-IR further suggests that hydrogenation of the formate species is the rate limiting step of methanol formation in UiO-67-Pt. Previously, an inverse KIE (albeit not as strong as in our case) was reported for CO_2 to methanol over $Cu/ZnO/Al_2O_3$, Cu/SiO_2, Cu/MgO, and Pd/SiO_2.[10] In that case, DFT calculations predicted an inverse KIE for hydrogenation of the formate species, in line with our results. A schematic presentation of the postulated reaction mechanism is shown in Scheme 2.

The integration of the $^{13}C/^{12}C$ transient response of methanol showed an intermediate species concentration of 23 μmol/g (Table 3), i.e., close to half the amount of Pt surface species estimated for the ensemble of Pt NPs identified by TEM (3.6 nm average diameter, Table 1). The schematic illustration of such a particle embedded in the MOF structure suggests that the average Pt NP contains 640 surface Pt sites and is surrounded by 32 Zr nodes that have a total of 224 Zr sites accessible for coordination at the Pt−MOF interface, corresponding to 112 bidentate formate species (Scheme 1, Figure 2). These numbers yield a formate-to-Pt surface site ratio of 112:640 (0.2), substantially lower than the estimated 23:55 (0.4) ratio from transient experiments.

Importantly, the numbers imply that additional Zr sites are available to formate formation around each Pt NP. In this respect, we hypothesized that Zr sites might become accessible by breaking Zr−linker bonds, either during Pt NP formation or during the catalytic reaction. The hypotheses were investigated by periodic DFT calculations (see the Experimental Details section for a brief description of the methodology and the

Supporting Information for further computational details and model construction). A Pt_{89} NP occupying the tetrahedral cavity of UiO-67 (Figure S18), Pt_{89}^{tet}, was found to be an adequate model, justified by the assumption that the interface between the Pt NP and the linker/Zr node is similar when the NP has a diameter of 3.6 nm or ≈1 nm.

In the perfect MOF structure, all 24 coordination sites of each Zr node are occupied by the carboxylate groups of the linker molecules (L). We first investigated the opening of such sites and computed the free energy profile of the system when a linker decoordinates from the node and slides along the Pt NP surface (Figures 4 and S22). Decoordination of the linker presumably occurs via $\sigma(Csp^2-Csp^2)$ bond rotation at the O_2C-C(Aryl) fragment, which generally involves low energy barriers. In Figure 4, L^X and O_2^X indicates the coordination mode of the linker or formate oxygen to the Zr node (X = number of Zr−O bonds) and * indicates the atom adsorbed to the Pt_{89} NP. These calculations showed that it is unfavorable to open two Zr sites ($\Delta G(L^2 \rightarrow L^0)$ = 16 kJ/mol), while opening one Zr site is favorable ($\Delta G(L^2 \rightarrow L^1)$ = −54 kJ/mol), indicating that the interaction with the NP weakens the node-linker Zr−O bonds, favoring the formation of vacant sites. Considering next the catalytic reaction, the first step of formate formation is the adsorption of a CO_2 molecule, which was found to coordinate its C atom to the Pt surface and the O atom to the opened Zr site ($\Delta G_{ads}(L^1 + CO_2 \rightarrow L^1-C^*O_2^1)$ = −20 kJ/mol) (Figure 4). When the formate formation pathway is continued from the $L^1-C^*O_2$ intermediate, the two subsequent intermediates, $L^1-C^*O_2^1 + 2H^*$, $\Delta G(L^2 + CO_2 + H_2 \rightarrow L^1-C^*O_2^1 + 2H^*)$ = −144 kJ/mol, and $L^1-HCO_2^1 + H^*$, $\Delta G(L^2 + CO_2 + H_2 \rightarrow L^1-HCO_2^1 + H^*)$ = −107 kJ/mol, correspond to H_2 adsorption on the Pt NP and a formate + hydride species, respectively (Figure 4). The H_2 adsorption is exergonic by −70 kJ/mol, and the subsequent H transfer to the C atom of CO_2 is endergonic by 37 kJ/mol. Interestingly, the transformation from $L^1-HCO_2^1 + H^*$ to $L^0-HCO_2^2 + H^*$, where the formate species is coordinated to two Zr sites is highly endergonic, $\Delta G_r(L^1-HCO_2^1 + H^* \rightarrow L^0-HCO_2^2 + H^*)$ = 78 kJ/mol. The transformation from $L^1-HCO_2^1 + H^*$ to $L^0-HCO_2^2 + H^*$ comprises two structural changes: (i) The formate moiety goes from being coordinating to one Zr site to being coordinated to two Zr sites; (ii) the linker decoordinates from one Zr site, opening two Zr sites. To estimate the contribution to the free energy change, $\Delta G(L^1-HCO_2^1 + H^* \rightarrow L^0-HCO_2^2 + H^*)$, of (i) and (ii), a computational experiment was performed: while keeping the linker in a "completely open position" (L^0), the formate moiety was oriented to its Zr-monodentate configuration HCO_2^1. This resulted in a potential energy increase of 45 kJ/mol.

These results indicate that the coordination of formate by one Zr−O bond (monodentate) is thermodynamically
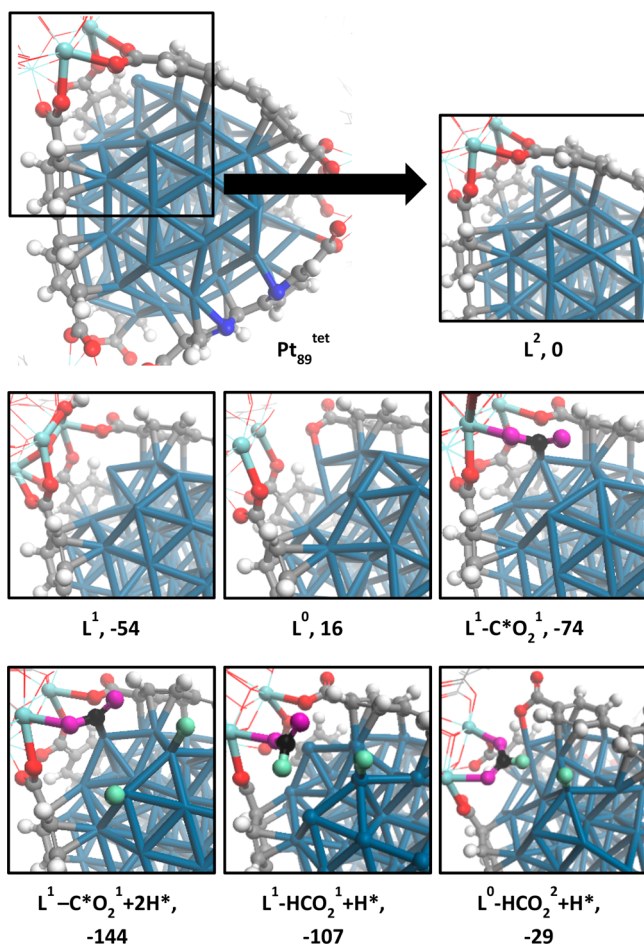
Figure 4. 3D representations of the intermediates of the reaction pathway toward the formation of the formate species coordinated to two Zr sites. Values are free energies in kJ/mol. L^X and O_2^X indicate the coordination number of the linker and formate to the Zr node and *, the atom adsorbed to Pt. O, C, and H atoms from CO_2 and H_2 are in pink, black, and green, and for the linker, they are in red, gray, and white.

species have been generated in Zr nodes with empty coordination sites at the start of the reaction, as represented in Scheme 2.

It was then explored whether the growth of the Pt NP during activation could cause the formation of such Zr nodes with open coordination sites. Insight into this possibility was obtained by computing the free energy of the Pt particle growth from Pt_{55}^{tet} to Pt_{89}^{tet}. These calculations showed that the reaction free energy of the system decreases as the Pt NP grows, and the decrease in energy will eventually exceed the energy loss of linker detachment (Figures S19−S21). Thus, during the nanoparticle growth, linkers will detach from the Zr nodes, and the Zr nodes will decorate the growing Pt nanoparticle. Returning to Scheme 1, the number of Zr nodes that needs to be removed from a perfect MOF lattice in order to create the 3.6 nm model Pt NP is a minimum of 6. The corresponding number of additional bidentate formate sites is 54. In combination with the 112 formate sites of the surrounding framework bound nodes, this yields a total number of formate sites of 166 and a formate-to-Pt surface atom ratio of 0.3, in reasonable agreement with the experimentally observed numbers.

Support for the computational results were found from online mass spectrometry (MS) measurements performed during activation in a 10% H_2/Ar atmosphere at 350 °C. The MS data revealed traces of phenyl-containing fragments in the effluent gas, suggesting that modulator and/or linker molecules desorbed from the material during Pt NP formation (Figure S8). The crystallographic features of the material were unchanged (Figures S2, S5, and S6) and the BPYDC/BPDC ratio remained constant during subsequent testing (Table S2). Furthermore, no linker fragments were observed during a second activation of UiO-67-Pt after testing, in line with the excellent catalyst stability observed under the reaction conditions.

Having established the importance of the Zr nodes and formate intermediates for methanol formation over UiO-67-Pt, the next issue is whether methanol formation could be decoupled from CO and CH_4 formation, hence, optionally leading to higher methanol selectivity. To this end, we first turn to classical kinetic experiments.

Contact time variation experiments, under otherwise constant conditions, showed that methanol selectivity is constant when CO_2 conversion increases, suggesting that it is a primary reaction product (Figure 5). Conversely, methane
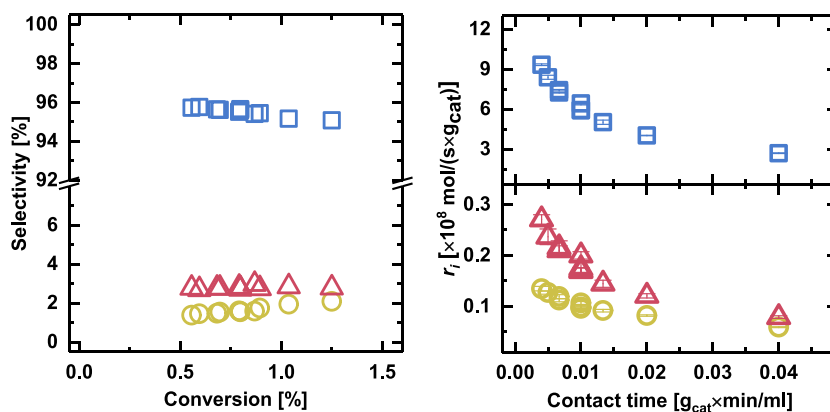
preferred in nodes initially saturated by linkers (L^2), while the coordination of formate by two Zr−O bonds (bidentate) is thermodynamically preferred in nodes initially having lost some linkers (L^0). Therefore, the observation of the latter coordination mode of formate by FT-IR suggests that these

Figure 5. Contact time variation during CO_2 hydrogenation to CO (squares), CH_4 (circles), and CH_3OH (triangles) at 170 °C, 1 bar, CO_2/H_2/He = 1/6/3, and τ = 0.004−0.04 g_{cat}·min/mL. (Left) Selectivity versus conversion. (Right) Rate of product formation versus contact time.

selectivity increases with increasing CO_2 conversion, while CO selectivity decreases, suggesting that CH_4 is mainly a secondary product, formed via CO. The latter result is in accordance with our previous studies of an analogous catalyst at higher temperature.[17]

Next, partial pressure variation experiments were performed in order to assess the reaction orders for each product. This assessment was complicated by the decreased formation rate of all the products with increasing contact time (Figure 5), indicating a strong adsorption of one or several reaction products, thereby poisoning the active site(s).[10,19] Indeed, when the rate decrease was correlated with the partial pressures of the majority products, CO and H_2O, all products had a reaction order close to negative 1 in p(CO + H_2O) and CH_4 was slightly less negative (Figure S10 and Table 2). On

Table 2. Reaction Orders in Total Pressure (p_{total}) and in pH_2, pCO_2, and p(CO + H_2O) (1 bar) for the Rate of Conversion (X) and CO, CH_4, and CH_3OH Formation at 170 °C over UiO-67-Pt

p_i	X	CO	CH_4	CH_3OH
p_{total}	0.1	0	0.3	1.1
CO + H_2O[a]	−1.1	−1.1	−0.7	−1
H_2[b]	0.2	0.2	0.9	1.7
CO_2[b]	0.9	0.9	0.1	0.7

[a]Estimated from contact time variation experiments (Figures 5 and S10). The reaction orders represent the average of two experiments. [b]Reaction orders when taking into account variable pCO and pH_2O in the reactor.

the basis of the FT-IR results reported above, it was shown that CO adsorbed on Pt (2042 cm^{-1})[17] dominates the Pt surface under the respective reaction conditions and CO was assessed as the main contributor to the inhibition, likely suppressing the coverage in H by competitive adsorption.[8] When taking into account the variable concentration of CO and H_2O, positive reaction orders in pH_2 and pCO_2 were observed for all products but with substantial differences (Table 2).

Considering first the majority product, CO, its formation rate depends strongly on pCO_2 but less on pH_2 (Table 2). Furthermore, no KIE was observed for CO during the (CO_2 + H_2)/(CO_2 + D_2) transient experiment (Table S5 and Figure S14), showing that breaking or making H−H or H−O bonds (which would otherwise lead to a primary KIE)[10,55] is not rate-determining for CO formation under the conditions studied here. Finally, the number of surface intermediates leading to CO formation and their mean residence time were calculated from the $^{13}C/^{12}C$ transients (Table 3 and Figure 3). The normalized ^{13}CO signal rapidly decreased to around 0.05 within the first 15 min and then slowly reached zero in the following 150 min. It is interesting to note that the number of

Table 3. Mean Surface Residence Times τ_{res} and the Number N_{ad} of Surface Intermediates Leading to the Formation of ^{13}CO, $^{13}CD_4$, and $^{13}CD_3OD$ at 170 °C (1 bar)[a]

	INT(CO)	INT(CD_4)	INT(CD_3OD)
N_{ads} ($\mu mol/g_{cat}$)	26 ± 3	3 ± 0.3	23 ± 2
τ_{res} (s)	0.5×10^3	2.1×10^3	3.8×10^3

[a]Calculated from integration of the curves in Figure 3 and the isotope-independent steady-state reaction rates.

surface intermediates leading to CO formation represents half of the Pt surface atoms in Pt NPs, estimated from TEM measurements (Table 1 vs Table 3). This observation, in combination with the partial coverage of the Pt NPs by Zr nodes (and linkers), the inhibiting effect of CO, the high predicted barrier of CO desorption from Pt,[18] and the observation of a positive correlation between facile CO desorption and the rate of CO formation in our previous study[17] strongly suggest CO desorption as the rate-limiting step in the RWGS reaction over UiO-67-Pt.

Turning next to the methane formation rate, it depends strongly on pH_2 and weakly on pCO_2 (Table 2). When one considers the high coverage of CO as well as the presumed indirect formation of methane via CO, this result is not surprising. In the (CO_2 + H_2)/(CO_2 + D_2) transient experiment, an inverse KIE of 0.6, i.e., intermediate between CO (KIE = 1) and methanol (KIE = 0.36), was observed for methane (Table S5 and Figure S14). Intriguingly, the inverse KIE was installed within the 15 min resolution of the gas analysis; hence, it was much more rapid than the transient behavior of methanol (Figure S14). Thus, the rate-determining step of methane formation involves bonding with hydrogen,[55−58] but the rate-determining step is not the same as for methanol formation. Indeed, the much more rapid transient behavior of methane compared to formate disqualifies formate as a significant intermediate to methane formation. This result implies that, except for hydrogen activation, methane formation is mechanistically decoupled from methanol formation. The normalized CH_4 formation rate (represented by the m/z = 15 signal of CH_3) also decreases rapidly to zero (comparable to H_2) during the H/D exchange (Figure 3). Due to their mass overlap with the much more abundant water fragments, the time evolution of partially exchanged methane/methyl species could not be followed. The transient behavior of methane during the $^{13}C/^{12}C$ switch (Figure 3) was markedly different from that observed in the H/D transient: The normalized $^{13}CD_4$ formation rate decreased to 0.5 during the first 7 min and then slowly to zero in the following 160 min. This distinct shape of the isotope transient indicates methane formation from two pools in parallel:[52,59] one rapidly converted to products, and the other converted more slowly. The integration of the transient curve showed that the number of surface intermediates leading to methane formation is low (Table 3). Moreover, about 3% of the methane-forming intermediates react fast and is responsible for about 50% of the steady-state methane formation rate, while the other 97% react slowly (Table 3 and Figure S15).

Returning finally to methanol, its formation depends strongly on both reactant partial pressures, in line with the observation that it is a primary product formed independently of CO (Figure 5). The $^{13}C/^{12}C$ transient experiment shows that methanol is formed from a similar number of surface intermediates as CO, but their turnover rate is much slower, hence leading to the 9% methanol selectivity observed under the respective conditions (Table 3).

Finally, the noncarbon products HD, H_2O, and HDO exhibited slow or partially slow transient responses (Figure 3). HD has a sharp initial peak with considerable tailing over the course of the following hour, indicating the formation from parallel pools and/or exchange with hydrogen-containing surface species.[60] H_2O showed transient characteristics suggestive of parallel pools, similar to CO and CH_4, and the HDO signal increased rapidly to a maximum within a few

minutes and then slowly decreased over the course of 2 h, closely following the methanol signal. The long surface lifetime of these products is indicative of a long-lived source of H participating in their formation, presumably also in the formation of methanol. Interestingly, quantification of the mol H in HD, H_2O, HDO, and CH_3OH yields 1500 μmol H per gram catalyst, which corresponds to about 80% of the theoretical amount of $Zr-\mu_3$-OH groups in the sample (HD accounts for 70%, as reported above).

CONCLUSION

Mechanistic aspects of CO_2 hydrogenation over UiO-67-Pt and the role of the UiO-67 framework have been investigated in detail by the employment of steady-state and transient kinetic studies, coupled with operando infrared spectroscopy and DFT modeling.

It was observed that Pt NPs embedded in the MOF structure are responsible for hydrogen activation and that formate species are formed at the Zr nodes by the reaction between adsorbed CO_2 and hydrogen spillover from an adjacent Pt NP. These results demonstrate that the Pt NPs strongly interact with defect Zr nodes during the reaction and, hence, that Zr nodes decorate the surface of the Pt NPs. Formate species are the most abundant intermediates in the reaction path to methanol, and transient results suggest that formate hydrogenation is the rate-limiting step of methanol formation. Importantly, the abundance of formate species is limited by the number of Zr sites made available by linker detachment due to Pt NP growth during catalyst activation.

CO and methane formation are mechanistically separated from methanol formation, except for the hydrogen dissociation step. The main route to methane formation is proposed as CO hydrogenation. Moreover, the presented data are consistent with CO desorption being the rate limiting step of the reverse water gas shift reaction over UiO-67-Pt.

ASSOCIATED CONTENT

Ⓢ Supporting Information

The Supporting Information is available free of charge at https://pubs.acs.org/doi/10.1021/jacs.9b10873.

Catalyst preparation, characterization, catalytic testing, operando FTIR, and computational details (PDF)

Cif files for computaitonal models in SI (ZIP)

Cif-files for computational models in main manuscript (ZIP)

AUTHOR INFORMATION

Corresponding Author

*unni.olsbye@kjemi.uio.no

ORCID ⊙

Andrea Lazzarini: 0000-0002-0404-6597

Torstein Fjermestad: 0000-0002-0363-3298

Maela Manzoli: 0000-0002-4427-7939

Silvia Bordiga: 0000-0003-2371-4156

Stian Svelle: 0000-0002-7468-5546

Egill Skúlason: 0000-0002-0724-680X

Ainara Nova: 0000-0003-3368-7702

Unni Olsbye: 0000-0003-3693-2857

Notes

The authors declare no competing financial interest.

REFERENCES

(1) Bellotti, D.; Rivarolo, M.; Magistri, L.; Massardo, A. F. Feasibility study of methanol production plant from hydrogen and captured carbon dioxide. *J. CO2 Util.* **2017**, *21*, 132−138.

(2) Chu, S.; Cui, Y.; Liu, N. The path towards sustainable energy. *Nat. Mater.* **2017**, *16*, 16.

(3) Olah, G. A. Beyond Oil and Gas: The Methanol Economy. *Angew. Chem., Int. Ed.* **2005**, *44* (18), 2636−2639.

(4) Porosoff, M. D.; Yan, B.; Chen, J. G. Catalytic reduction of CO2 by H2 for synthesis of CO, methanol and hydrocarbons: challenges and opportunities. *Energy Environ. Sci.* **2016**, *9* (1), 62−73.

(5) Wang, W.; Wang, S.; Ma, X.; Gong, J. Recent advances in catalytic hydrogenation of carbon dioxide. *Chem. Soc. Rev.* **2011**, *40* (7), 3703−3727.

(6) Li, W.; Wang, H.; Jiang, X.; Zhu, J.; Liu, Z.; Guo, X.; Song, C. A short review of recent advances in CO2 hydrogenation to hydro-carbons over heterogeneous catalysts. *RSC Adv.* **2018**, *8* (14), 7651−7669.

(7) Kattel, S.; Liu, P.; Chen, J. G. Tuning Selectivity of CO2 Hydrogenation Reactions at the Metal/Oxide Interface. *J. Am. Chem. Soc.* **2017**, *139* (29), 9739−9754.

(8) Wang, X.; Shi, H.; Kwak, J. H.; Szanyi, J. Mechanism of CO2 Hydrogenation on Pd/Al2O3 Catalysts: Kinetics and Transient DRIFTS-MS Studies. *ACS Catal.* **2015**, *5* (11), 6337−6349.

(9) Wu, H. C.; Chang, Y. C.; Wu, J. H.; Lin, J. H.; Lin, I. K.; Chen, C. S. Methanation of CO2 and reverse water gas shift reactions on Ni/SiO2 catalysts: the influence of particle size on selectivity and reaction pathway. *Catal. Sci. Technol.* **2015**, *5* (8), 4154−4163.

(10) Kunkes, E. L.; Studt, F.; Abild-Pedersen, F.; Schlögl, R.; Behrens, M. Hydrogenation of CO2 to methanol and CO on Cu/ZnO/Al2O3: Is there a common intermediate or not? *J. Catal.* **2015**, *328*, 43−48.

(11) Chen, X.; Su, X.; Duan, H.; Liang, B.; Huang, Y.; Zhang, T. Catalytic performance of the Pt/TiO2 catalysts in reverse water gas shift reaction: Controlled product selectivity and a mechanism study. *Catal. Today* **2017**, *281*, 312−318.

(12) Hartadi, Y.; Widmann, D.; Behm, R. J. Methanol formation by CO2 hydrogenation on Au/ZnO catalysts − Effect of total pressure and influence of CO on the reaction characteristics. *J. Catal.* **2016**, *333*, 238−250.

(13) Gaikwad, R.; Bansode, A.; Urakawa, A. High-pressure advantages in stoichiometric hydrogenation of carbon dioxide to methanol. *J. Catal.* **2016**, *343*, 127−132.

(14) Román-Martínez, M. C.; Cazorla-Amorós, D.; Linares-Solano, A.; Salinas-Martínez de Lecea, C. CO2 hydrogenation under pressure on catalysts Pt—Ca/C. *Appl. Catal., A* **1996**, *134* (1), 159−167.

(15) Kim, S. S.; Park, K. H.; Hong, S. C. A study of the selectivity of the reverse water−gas-shift reaction over Pt/TiO2 catalysts. *Fuel Process. Technol.* **2013**, *108*, 47−54.

(16) Goguet, A.; Meunier, F. C.; Tibiletti, D.; Breen, J. P.; Burch, R. Spectrokinetic investigation of reverse water-gas-shift reaction intermediates over a Pt/CeO2 catalyst. *J. Phys. Chem. B* **2004**, *108* (52), 20240−20246.

(17) Gutterød, E. S.; Øien-Ødegaard, S.; Bossers, K.; Nieuwelink, A.-E.; Manzoli, M.; Braglia, L.; Lazzarini, A.; Borfecchia, E.; Ahmadigoltapeh, S.; Bouchevreau, B.; Lønstad-Bleken, B. T.; Henry, R.; Lamberti, C.; Bordiga, S.; Weckhuysen, B. M.; Lillerud, K. P.; Olsbye, U. CO2 Hydrogenation over Pt-Containing UiO-67 Zr-MOFs—The Base Case. *Ind. Eng. Chem. Res.* **2017**, *56* (45), 13206−13218.

(18) Kattel, S.; Yan, B.; Chen, J. G.; Liu, P. CO2 hydrogenation on Pt, Pt/SiO2 and Pt/TiO2: Importance of synergy between Pt and oxide support. *J. Catal.* **2016**, *343*, 115−126.

(19) Kim, S. S.; Lee, H. H.; Hong, S. C. A study on the effect of support's reducibility on the reverse water-gas shift reaction over Pt catalysts. *Appl. Catal., A* **2012**, *423*, 100−107.

(20) Tibiletti, D.; Goguet, A.; Meunier, F. C.; Breen, J. P.; Burch, R. On the importance of steady-state isotopic techniques for the investigation of the mechanism of the reverse water-gas-shift reaction. *Chem. Commun.* **2004**, No. 14, 1636−1637.

(21) Jacobs, G.; Davis, B. H. Reverse water-gas shift reaction: steady state isotope switching study of the reverse water-gas shift reaction using in situ DRIFTS and a Pt/ceria catalyst. *Appl. Catal., A* **2005**, *284* (1), 31−38.

(22) Kalamaras, C. M.; Panagiotopoulou, P.; Kondarides, D. I.; Efstathiou, A. M. Kinetic and mechanistic studies of the water−gas shift reaction on Pt/TiO2 catalyst. *J. Catal.* **2009**, *264* (2), 117−129.

(23) Burch, R.; Goguet, A.; Meunier, F. C. A critical analysis of the experimental evidence for and against a formate mechanism for high activity water-gas shift catalysts. *Appl. Catal., A* **2011**, *409−410*, 3−12.

(24) Kalamaras, C. M.; Olympiou, G. G.; Efstathiou, A. M. The water-gas shift reaction on Pt/γ-Al2O3 catalyst: Operando SSITKA-DRIFTS-mass spectroscopy studies. *Catal. Today* **2008**, *138* (3), 228−234.

(25) Ouyang, B.; Xiong, S.; Zhang, Y.; Liu, B.; Li, J. The study of morphology effect of Pt/Co3O4 catalysts for higher alcohol synthesis from CO2 hydrogenation. *Appl. Catal., A* **2017**, *543*, 189−195.

(26) Sápi, A.; Rajkumar, T.; Ábel, M.; Efremova, A.; Grósz, A.; Gyuris, A.; Ábrahámné, K. B.; Szenti, I.; Kiss, J.; Varga, T.; Kukovecz, Á.; Kónya, Z. Noble-metal-free and Pt nanoparticles-loaded, mesoporous oxides as efficient catalysts for CO2 hydrogenation and dry reforming with methane. *J. CO2 Util.* **2019**, *32*, 106−118.

(27) Liu, B.; Ouyang, B.; Zhang, Y.; Lv, K.; Li, Q.; Ding, Y.; Li, J. Effects of mesoporous structure and Pt promoter on the activity of Co-based catalysts in low-temperature CO2 hydrogenation for higher alcohol synthesis. *J. Catal.* **2018**, *366*, 91−97.

(28) Inoue, T.; Iizuka, T. Hydrogenation of carbon dioxide and carbon monoxide over supported platinum catalysts. *J. Chem. Soc., Faraday Trans. 1* **1986**, *82* (6), 1681−1686.

(29) Rungtaweevoranit, B.; Baek, J.; Araujo, J. R.; Archanjo, B. S.; Choi, K. M.; Yaghi, O. M.; Somorjai, G. A. Copper Nanocrystals Encapsulated in Zr-based Metal−Organic Frameworks for Highly Selective CO2 Hydrogenation to Methanol. *Nano Lett.* **2016**, *16* (12), 7645−7649.

(30) An, B.; Zhang, J.; Cheng, K.; Ji, P.; Wang, C.; Lin, W. Confinement of Ultrasmall Cu/ZnOx Nanoparticles in Metal−Organic Frameworks for Selective Methanol Synthesis from Catalytic Hydrogenation of CO2. *J. Am. Chem. Soc.* **2017**, *139* (10), 3834−3840.

(31) Lippert, G.; Hutter, J.; Parrinello, M. The Gaussian and augmented-plane-wave density functional method for ab initio molecular dynamics simulations. *Theor. Chem. Acc.* **1999**, *103*, 124−140.

(32) Lippert, G.; Hutter, J.; Parrinello, M. A hybrid Gaussian and plane wave density functional scheme. *Mol. Phys.* **1997**, *92* (3), 477−487.

(33) VandeVondele, J.; Krack, M.; Mohamed, F.; et al. Quickstep: Fast and accurate density functional calculations using a mixed Gaussian and plane waves approach. *Comput. Phys. Commun.* **2005**, *167*, 103−128.

(34) CP2K Developers Group. *CP2K*, version 6.1; 2018.

(35) Hutter, J.; Iannuzzi, M.; Schiffmann, F.; VandeVondele, J. CP2K: atomistic simulations of condensed matter systems. *WIREs Comput. Mol. Sci.* **2014**, *4*, 15−25.

(36) VandeVondele, J.; Hutter, J. Gaussian basis sets for accurate calculations on molecular systems in gas and condensed phases. *J. Chem. Phys.* **2007**, *127* (11), 114105.

(37) Kaur, G.; Øien-Ødegaard, S.; Lazzarini, A.; Chavan, S. M.; Bordiga, S.; Lillerud, K. P.; Olsbye, U. Controlling the Synthesis of Metal−Organic Framework UiO-67 by Tuning Its Kinetic Driving Force. *Cryst. Growth Des.* **2019**, *19* (8), 4246−4251.

(38) Wu, H.; Chua, Y. S.; Krungleviciute, V.; Tyagi, M.; Chen, P.; Yildirim, T.; Zhou, W. Unusual and Highly Tunable Missing-Linker Defects in Zirconium Metal−Organic Framework UiO-66 and Their Important Effects on Gas Adsorption. *J. Am. Chem. Soc.* **2013**, *135* (28), 10525−10532.

(39) Yang, D.; Ortuño, M. A.; Bernales, V.; Cramer, C. J.; Gagliardi, L.; Gates, B. C. Structure and Dynamics of Zr6O8Metal−Organic Framework Node Surfaces Probed with Ethanol Dehydration as a Catalytic Test Reaction. *J. Am. Chem. Soc.* **2018**, *140* (10), 3751−3759.

(40) Shearer, G. C.; Chavan, S.; Bordiga, S.; Svelle, S.; Olsbye, U.; Lillerud, K. P. Defect Engineering: Tuning the Porosity and Composition of the Metal−Organic Framework UiO-66 via Modulated Synthesis. *Chem. Mater.* **2016**, *28* (11), 3749−3761.

(41) Feng, L.; Yuan, S.; Zhang, L.-L.; Tan, K.; Li, J.-L.; Kirchon, A.; Liu, L.-M.; Zhang, P.; Han, Y.; Chabal, Y. J.; Zhou, H.-C. Creating Hierarchical Pores by Controlled Linker Thermolysis in Multivariate Metal−Organic Frameworks. *J. Am. Chem. Soc.* **2018**, *140* (6), 2363−2372.

(42) Shearer, G. C.; Chavan, S.; Ethiraj, J.; Vitillo, J. G.; Svelle, S.; Olsbye, U.; Lamberti, C.; Bordiga, S.; Lillerud, K. P. Tuned to Perfection: Ironing Out the Defects in Metal−Organic Framework UiO-66. *Chem. Mater.* **2014**, *26* (14), 4068−4071.

(43) Shearer, G. C.; Forselv, S.; Chavan, S.; Bordiga, S.; Mathisen, K.; Bjørgen, M.; Svelle, S.; Lillerud, K. P. In Situ Infrared Spectroscopic and Gravimetric Characterisation of the Solvent Removal and Dehydroxylation of the Metal Organic Frameworks UiO-66 and UiO-67. *Top. Catal.* **2013**, *56* (9), 770−782.

(44) Trickett, C. A.; Gagnon, K. J.; Lee, S.; Gándara, F.; Bürgi, H.-B.; Yaghi, O. M. Definitive Molecular Level Characterization of Defects in UiO-66 Crystals. *Angew. Chem., Int. Ed.* **2015**, *54* (38), 11162−11167.

(45) Øien, S.; Wragg, D.; Reinsch, H.; Svelle, S.; Bordiga, S.; Lamberti, C.; Lillerud, K. P. Detailed Structure Analysis of Atomic Positions and Defects in Zirconium Metal−Organic Frameworks. *Cryst. Growth Des.* **2014**, *14* (11), 5370−5372.

(46) Braglia, L.; Borfecchia, E.; Lomachenko, K. A.; Bugaev, A. L.; Guda, A. A.; Soldatov, A. V.; Bleken, B. T. L.; Oien, S.; Olsbye, U.; Lillerud, K. P.; Bordiga, S.; Agostini, G.; Manzoli, M.; Lamberti, C. Tuning Pt and Cu sites population inside functionalized UiO-67 MOF by controlling activation conditions. *Faraday Discuss.* **2017**, *201*, 265−286.

(47) Øien, S.; Agostini, G.; Svelle, S.; Borfecchia, E.; Lomachenko, K. A.; Mino, L.; Gallo, E.; Bordiga, S.; Olsbye, U.; Lillerud, K. P.; Lamberti, C. Probing Reactive Platinum Sites in UiO-67 Zirconium Metal−Organic Frameworks. *Chem. Mater.* **2015**, *27* (3), 1042−1056.

(48) Braglia, L.; Borfecchia, E.; Martini, A.; Bugaev, A. L.; Soldatov, A. V.; Øien-Ødegaard, S.; Lønstad-Bleken, B. T.; Olsbye, U.; Lillerud, K. P.; Lomachenko, K. A.; Agostini, G.; Manzoli, M.; Lamberti, C. The duality of UiO-67-Pt MOFs: connecting treatment conditions and encapsulated Pt species by operando XAS. *Phys. Chem. Chem. Phys.* **2017**, *19* (40), 27489−27507.

(49) Wang, X.; Shi, H.; Szanyi, J. Controlling selectivities in CO2 reduction through mechanistic understanding. *Nat. Commun.* **2017**, *8* (1), 513.

(50) Busca, G.; Lamotte, J.; Lavalley, J. C.; Lorenzelli, V. FT-IR study of the adsorption and transformation of formaldehyde on oxide surfaces. *J. Am. Chem. Soc.* **1987**, *109* (17), 5197−5202.

(51) Tibiletti, D.; Meunier, F. C.; Goguet, A.; Reid, D.; Burch, R.; Boaro, M.; Vicario, M.; Trovarelli, A. An investigation of possible mechanisms for the water−gas shift reaction over a ZrO2-supported Pt catalyst. *J. Catal.* **2006**, *244* (2), 183−191.

(52) Ledesma, C.; Yang, J.; Chen, D.; Holmen, A. Recent Approaches in Mechanistic and Kinetic Studies of Catalytic Reactions Using SSITKA Technique. *ACS Catal.* **2014**, *4* (12), 4527−4547.

(53) Lowry, T. H.; Richardson, K. S. *Mechanism and Theory in Organic Chemistry*; Harper & Row, 1987.

(54) Larmier, K.; Liao, W.-C.; Tada, S.; Lam, E.; Verel, R.; Bansode, A.; Urakawa, A.; Comas-Vives, A.; Copéret, C. CO2-to-Methanol Hydrogenation on Zirconia-Supported Copper Nanoparticles: Reaction Intermediates and the Role of the Metal−Support Interface. *Angew. Chem., Int. Ed.* **2017**, *56* (9), 2318−2323.

(55) Ojeda, M.; Li, A.; Nabar, R.; Nilekar, A. U.; Mavrikakis, M.; Iglesia, E. Kinetically Relevant Steps and H2/D2 Isotope Effects in Fischer−Tropsch Synthesis on Fe and Co Catalysts. *J. Phys. Chem. C* **2010**, *114* (46), 19761−19770.

(56) Watson, D. T. P.; Ge, Q.; King, D. A. Facile H−D exchange in adsorbed methylidyne on Pt{110}−(1 × 2) and deuteration to gaseous methane. *J. Chem. Phys.* **2001**, *115* (24), 11306−11316.

(57) Polanyi, M. Reaction Rates of the Hydrogen Isotopes. *Nature* **1934**, *133*, 26.

(58) Bawn, C. E. H.; Ogden, G. Wave mechanical effects and the reactivity of the hydrogen isotopes. *Trans. Faraday Soc.* **1934**, *30* (0), 432−443.

(59) Shannon, S. L.; Goodwin, J. G. Characterization of Catalytic Surfaces by Isotopic-Transient Kinetics during Steady-State Reaction. *Chem. Rev.* **1995**, *95* (3), 677−695.

(60) Xie, J.; Yang, J.; Dugulan, A. I.; Holmen, A.; Chen, D.; de Jong, K. P.; Louwerse, M. J. Size and Promoter Effects in Supported Iron Fischer−Tropsch Catalysts: Insights from Experiment and Theory. *ACS Catal.* **2016**, *6* (5), 3147−3157.